

# Electrical characterization of Colombian soils: A tool for detection of improvised explosive devices with Ground Penetrating Radar

Daniel Julián González Ramírez  
School of Electrical and Electronic Engineering  
Universidad de los Andes  
Colombia  
dj.gonzalez1203@uniandes.edu.co

Roberto Bustamante Miller  
School of Electrical and Electronic Engineering  
Universidad de los Andes  
Colombia  
rbustama@uniandes.edu.co

**Abstract**—Electrical characterization of Colombian soils is done to obtain their conductivity and complex permittivity. Permittivity and conductivity are determined by using TDR technique, to obtain a reflection waveform from a coaxial probe inserted in the soil, and by processing the waveform with different algorithms, including a PSO algorithm. An IED model is built in gprMax FDTD simulator and the performance of a GPR is evaluated through the simulation detection scenarios using a Debye relaxation model to represent the characterized soils. Soils from different regions show variations from one another on their dielectric behavior and therefore the performance of GPR as IED detector varies over the different soils.

**Keywords**—Colombian soil, electrical characterization, Debye relaxation, complex dielectric permittivity, electrical conductivity, ground penetrating radar (GPR), improvised explosive devices (IED), time domain reflectometry (TDR), finite difference time domain (FDTD), particle swarm optimization (PSO).

## I. INTRODUCTION

Antipersonnel mines are a humanitarian problem because they can seriously injure or kill civilians. Since mines are planted weapons, they do not see the difference between civilians and military, and can remain active for decades. Since 1997, international treaties have been made that seek a world free of antipersonnel mines; to achieve this, it is essential to be able to detect and neutralize them [1].

Improvised explosive devices (IEDs) are a type of handcrafted-artisan antipersonnel mines. The mechanisms of action, the materials and the geometry of the IED are varied therefore, there is a large number of IED configurations; including configurations with low and non-metallic content [2], [3]. In Colombia, insurgent groups typically use IEDs instead of conventional antipersonnel mines making IED detection of great importance for Colombia. Metal detectors and explosive detection dogs are the predominant methods used for the detection of antipersonnel mines. The large amount of IED configurations makes the metal detectors ineffective in many cases [2], [3]. Explosive detection dogs are very effective since the detection is made by detecting the odor from the explosives, but this technique also has several challenges including: exhaustion of the dogs because of long walks into

areas of difficult access, irregular emission of odor particles in swampy areas, and costs associated with training and maintenance, among others [3].

Ground penetrating radar (GPR) is an electromagnetic technique that surveys the ground for the location of buried objects [1]. GPR has applications in several science and engineering fields, mine detection is among these applications and has been extensively researched over the years. The overall detection results of GPR have proven the technique effective [4]–[6]. Nevertheless GPR has still detection problems mainly associated with the different type of soils where landmines are deployed [2], [7]. Given that there are limitless possible configurations of environment, weather and soil mineralogy the calibration and setup of GPR equipment and algorithms is a problem that needs to be addressed with a good soil characterization [7], [8].

Determining the usefulness of GPR for humanitarian demining in Colombia is done by the following:

- selection of a technique to measure the electrical response of soils in field;
- reproduction the measurement technique with gprMax electromagnetic simulator;
- development of an algorithm that determines electrical properties of soils based on the electrical response of given by the selected technique;
- validate the algorithms through a blind test with the results obtained from gprMax simulations;
- measurement of the electrical response of different Colombian soils with the selected technique;
- determination of the electrical properties of the soils (complex permittivity and conductivity) by processing the measurements with the developed algorithm and adjustment of the recovered properties to a relaxation model that can be introduced into gprMax;
- identification of geometry and materials of a typical IED and construction of an IED model into gprMax with variables sizes, material properties, and triggering mechanisms; and
- simulation of GPR surveys on the characterized soils and

the constructed IED obtaining A- and B-Scans.

This paper will first, give an introduction into the electrical properties of soils and its importance for GPR detection of IEDs. And later, show the followed procedure to fulfill each of the items listed previously for the determination of GPR usefulness for humanitarian demining in Colombia.

## II. ELECTRICAL PROPERTIES OF SOILS

Propagation of electromagnetic waves is described by the Maxwell equations (1) [9], the interaction between interfaces and propagation within mediums are defined by the electrical properties of the materials involved. The electrical properties of any material are permittivity ( $\epsilon$ ), conductivity ( $\sigma$ ) and permeability ( $\mu$ ). By knowing these properties, the Maxwell equations can be solved —usually with simulation using a numerical method— and the behaviour of the electromagnetic waves can be determined.

$$\begin{aligned} \nabla \cdot \vec{D} &= \rho_v & \nabla \cdot \vec{B} &= 0 & \nabla \times \vec{E} &= -\frac{\partial \vec{B}}{\partial t} \\ \nabla \times \vec{H} &= \vec{J}_{ic} + \frac{\partial \vec{D}}{\partial t} & \nabla \cdot \vec{J}_{ic} &= -\frac{\partial \rho_v}{\partial t} & \vec{J}_{ic} &= \vec{J}_i + \vec{J}_c \quad (1) \\ \vec{B} &= \bar{\mu} * \vec{H} & \vec{D} &= \bar{\epsilon} * \vec{E} & \vec{J}_c &= \bar{\sigma} * \vec{E} \end{aligned}$$

A GPR creates an electric signal in a wide range of frequencies and feeds them to antennas that generate electromagnetic waves, the waves interact with the objects in their path and the GPR senses the reflections from these interactions. The reflected waves will be affected by the geometry of the objects and the electrical properties of their composing materials. In an antipersonnel-landmine (APL) detection scenario with GPR, there are several objects with different materials and geometries that will interact with the electromagnetic waves such as: air, soil, vegetation, rocks and APLs. The attenuation of the reflected waves is key for GPR performance and a way to determine this parameter is by simulating the detection scenarios with the proper geometry and electrical properties of the objects involved.

Soil is one of the most important media when studying APL detection with GPR as it is the medium that holds the APLs. Therefore, to understand the propagation phenomena, a characterization of the soil electrical properties is due. Soils are a four-phase medium as shown in Fig. 1 comprehending a solid matrix and pores that contain: air, free water and bound water [10]. The solid matrix is the phase containing the solid particles of the minerals that make up the soil, these particles are of different sizes and are stacked, creating pores between them which are filled with air and water. Water is divided into two phases: free water and bound water. Bound water is the water adhered to the pores walls and free water is the water further away from the walls. Electrical properties of all the four phases are different, so the electrical properties of the soil are a mixture of the properties of each independent phase. The soil characterization that will be done over this paper will assume that relative permeability of soils as  $\mu_r = 1$  given that even soils with high content of ferrimagnetic minerals

have shown to have  $\mu_r < 1.1$  as stated by Igel [10]. The characterization of soils will therefore be of their conductivity and permittivity, the mechanisms that affect these properties are described following.

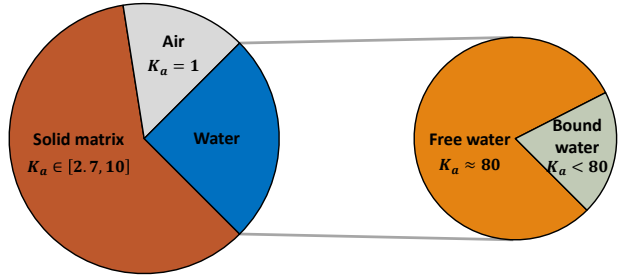


Figure 1. Soil as a four-phase medium. Typical proportion of the phases and apparent permittivity are shown.

### A. Conductivity

Solid matrix and water phases of a soil contribute to the electrical conductivity of it whereas air is assumed to be completely dielectric. There are three mechanisms that describe the electrical conductivity of soils [10]:

- **Electronic conductivity:** caused by the free electrons from the crystal lattice of the solid matrix minerals.
- **Electrolytic conductivity:** caused by the aqueous liquid in the pore space which feature dissolved ions.
- **Superficial conductivity:** caused by the cation exchange between the solid matrix and the pore fluids.

Through this paper the conductivity will be noted as  $\sigma_{DC}$  and will be assumed constant over frequency. This assumption is based on the normal behavior observed in soils [8], [11]–[13], as both electronic and electrolytic conductivity are independent from frequency and superficial conductivity is usually low compared to the other two mechanisms.

### B. Permittivity

Soils are polarized when exposed to an external electric field, this means that there is a displacement of the positive and negative charges from the molecules of the phases that make the soil up. Charges will align in the direction of the external field and will store energy in form of electric moment. Once the external field alternates or subsides the molecules will release this energy causing an opposite field and therefore a reduction of intensity over the total electric field in the material [11], [14].

Similarly to the conductivity each phase has an individual mechanism of polarization and therefore contributes to the overall permittivity of the soil in different ways. In Fig. 1 the typical values for apparent permittivity ( $K_a$ ) of each phase are shown, from the range of values it can be seen that water has a very high value of  $K_a$  in comparison with the other phases therefore the overall permittivity of a soil is governed mainly by its water content.

Air and the solid matrix have a frequency independent permittivity in the GPR frequency range, whereas water shows

a decrease of permittivity with increasing frequency. The frequency dependence is caused by the polarity of water molecules [14]. Because the molecules of the polar medium cannot align at the rate the external electrical field is alternating, stored energy is released as heat. The frequency at which the molecules cannot follow the electrical field is known as relaxation frequency  $f_{relax}$ . Permittivity dependence on frequency is called dispersion; as the propagation velocity of electromagnetic waves varies with frequency, resulting in a spread of waves over time.

The frequency dependent behavior is represented by the complex permittivity:  $\varepsilon_r^*(f) = \varepsilon'_r(f) - j\varepsilon''_r(f)$ . The real part of the permittivity ( $\varepsilon'_r$ ) represents the alignment of molecules towards the external electric field and the imaginary part ( $\varepsilon''_r$ ) represent the dielectric losses. As conductivity is a source of losses, often it is included into the imaginary part of permittivity as noted in Eq. (2), where  $\varepsilon_0 = 8.85 \times 10^{-12} \text{ F/m}$  is the vacuum permittivity.

$$\varepsilon_r^*(f) = \varepsilon'_r(f) - j \left[ \varepsilon''_r(f) + \frac{\sigma_{DC}}{2\pi f \varepsilon_0} \right] \quad (2)$$

Dispersive media is usually represented by a permittivity dispersion model such as Debye [14] and Cole-Cole [15] models. These models are special cases of the Havriliak-Negami model [16] in Eq. (3) where  $0 \leq \alpha \leq 1$  y  $\beta \leq 1$ ,  $\tau_0 = 1/(2\pi f_{relax})$  is the relaxation time,  $\varepsilon_s$  is the static permittivity, and  $\varepsilon_\infty$  is the permittivity at infinite frequency. In the Debye model:  $\alpha = 0$  and  $\beta = 1$ ; and in the Cole-Cole model:  $0 \leq \alpha \leq 1$  and  $\beta = 1$ .

$$\varepsilon_r^*(f) = \varepsilon_\infty + \frac{\varepsilon_s - \varepsilon_\infty}{[1 + (j2\pi f\tau_0)^{1-\alpha}]^\beta} - \frac{j\sigma_{DC}}{2\pi f \varepsilon_0} \quad (3)$$

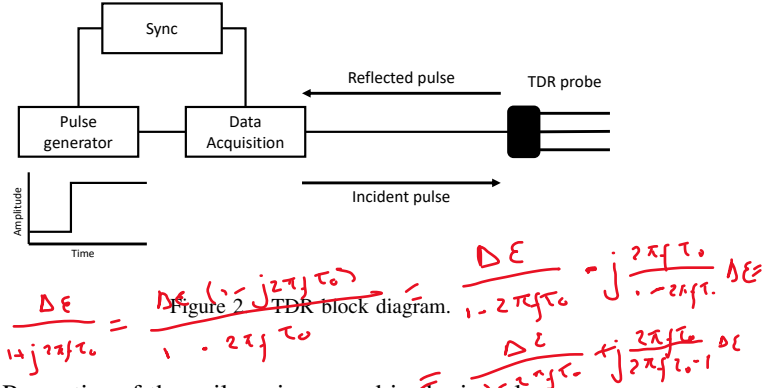
These models are useful when introducing dispersive media into electromagnetic simulators. For this paper: gprMax simulator [17] (which is based on the Finite-Difference Time-Domain (FDTD) method) is used to create GPR detection scenarios and to reproduce the measurement technique for soil characterization. Implementation of dispersive media on FDTD is easy through the Debye model, therefore this model will be used to represent the soil characterizations.

### III. SELECTION OF A TECHNIQUE FOR MEASURING THE ELECTRICAL RESPONSE OF SOILS

There are several techniques to obtain a complete characterization of dielectric materials, these techniques can be used to recover the permittivity and conductivity of soils allowing for inclusion of real soil models into gprMax simulator. Soil varies significantly with environment, weather, mineralogy and geography of different places [18] therefore is not accurate to characterize one soil type and assume every soil the same. Several techniques were considered upon to make the soil characterizations in different Colombian territories having in mind: that field measurements are preferred over sampling soils and making laboratory measurements, and the needed parameters are  $\varepsilon_r^*(f)$  and  $\sigma_{DC}$ . The considered techniques include: transmission/reflection line, open-ended coaxial probe,

free space, resonant cavity, ground wave, and time-domain reflectometry [10], [11], [19], [20]

Time-domain reflectometry (TDR) is the selected technique to make the soil characterization, which fulfills the criteria of allowing field measurements and obtaining conductivity and complex permittivity [11], [19]. TDR is a time domain technique that feeds square pulses with very short rise times to a TDR probe (coaxial probe) inserted in the target soil, the reflected pulse is then measured and stored. Reflections are caused by impedance mismatches and therefore they contain information on the electrical properties of the soil. A block diagram for the TDR measurements is shown in Fig. 2. The short rise times of the incident pulse allow for a wide frequency bandwidth which means a good characterization of soils over frequency. Electrical properties are recovered from the reflected pulse through time-domain analysis of the reflected waveform and frequency-domain analysis of the  $S_{11}$  scattering parameter, obtained through the Fourier transform of the time-domain waveforms.



Properties of the soil are immersed in the impulse response function  $s(t)$ , making it the function of interest for which the analysis should take place. But the impulse response function cannot be measured physically so it must be obtained from its relationship with the known signals: reflected voltage ( $r(t)$ ) and incident voltage ( $v_0(t)$ ). The relationship between these signals is given by Eq. (4), where  $R(f)$ ,  $V_0(f)$  and  $S(f)$  are the Fourier transforms of  $r(t)$ ,  $v_0(t)$  and  $s(t)$ .  $S(f)$  is known as the transfer function of the soil and has the same definition as the  $S_{11}$  parameter from the scattering matrix.

$$2\pi f\tau_0 > 2\pi f\tau_0 - \rightarrow C$$

$$r(t) = \int_{-\infty}^{\infty} v_0(t - \tau) s(\tau) d\tau \quad R(f) = V_0(f) S(f) \quad (4)$$

Both  $s(t)$  and  $S(f)$  are function of the electrical properties of the soil and the TDR probe. The TDR probes attempt to reproduce the frequency behavior of an open-ended coaxial transmission line filled with soil [21], the  $S_{11}$  scatter function for this transmission line is well known and is given by Eqs. (5) - (9) [19] for a probe filled with material of  $\varepsilon_r^*(f)$  permittivity.

$$S_{11}(f) = \frac{\rho^* + \exp(-2\gamma L)}{1 + \rho^* \exp(-2\gamma L)} \quad (5)$$

$$\rho^* = \frac{1 - z[\varepsilon_r^*(f)]^{1/2}}{1 + z[\varepsilon_r^*(f)]^{1/2}} \quad (6)$$

$$\gamma L = j2\pi f L \frac{[\varepsilon_r^*(f)]^{1/2}}{c_0} \quad (7)$$

$$z = \frac{Z_c}{Z_p} \quad (8)$$

$$Z_p = \frac{60}{\sqrt{\varepsilon_r^*}} \ln \frac{b}{a} \quad (9)$$

Figure 3 summarizes the parameters obtained from different analysis done over the TDR signal. Conductivity ( $\sigma_{DC}$ ), apparent permittivity ( $K_a$ ) and static permittivity ( $\varepsilon_s$ ) can be determined from the time-domain analysis of the reflected voltage and complex permittivity ( $\varepsilon_r^*(f)$ ) can be determined with the frequency-domain analysis and the data obtained from the time-domain analysis. In Section V the analysis over the signals will be explained in depth and the validation of the analysis will be shown in Section VI.

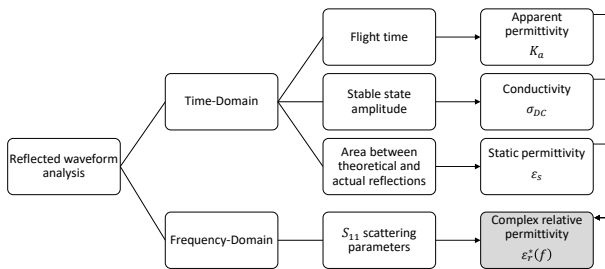


Figure 3. Summary of the analysis over the reflected waveform.

#### IV. CONSTRUCTION OF TDR AND MEASUREMENTS IN GPRMAX

For the better understanding on the phenomena behind TDR measurements and to provide a validation data-set, the TDR technique was reproduced in gprMax. To have a proper representation of real measurements the specifications of the TDR simulations were set as in Campbell Scientific TDR200 [22] and a probe similar to Campbell Scientific CS610 [23] was built into gprMax.

The first step to reproduce the TDR was building the incident waveform into a text file, with the proper rise time ( $t_{rise} = 85$  ps) and amplitude ( $v_{inc}(\infty) = 250$  mV). Two important considerations related with the FDTD algorithm had to be taken into account for the creation of the pulse: the rise time of the pulse should be represented by at least  $10 \times \Delta t$  and there should be a considerable delay before the rise flank of the pulse at least  $6 \times t_{rise}$ , satisfying these conditions guarantees stability for the simulation as there should not be abrupt changes in voltages. The generated pulse will be added to the model through a method that allows to apply the incident voltage and then calculate the reflected waveform in the feeding transmission line proposed by Maloney et. al [24],

this can be done through the creation of a 1-D FDTD grid that connects to the 3-D grid of the main model. In this alternate 1-D grid a one-way injector is placed to feed the voltage into the main grid and the reflected voltage is measured after the one-way injector. This transmission line model is included as a native command for gprMax so the implementation is done through one command line.

Then a coaxial cable is built so the impedance matches the  $50 \Omega$  of the feeding transmission line. One approach to this was using the dimensions of the RG-8 cable [25] that feeds the CS610 probe, this showed bad results as the spatial resolution (1 mm) proved to be too coarse to properly represent the cylinders that made up the cable (resolution was set at a minimum of 1 mm because of the computational resources available). So a modified version of the cable was created looking to accomplish the  $50 \Omega$  impedance. The resulting cable is shown in Fig. 4 where: the inner conductor diameter  $a = 4$  mm, the outer conductor distance  $b = 12$  mm and  $\varepsilon_{cable} = 2.4$ . A simple voltage source of  $50 \Omega$  impedance and 500 mV amplitude was connected to one end of this cable and a  $50 \Omega$  load to the other end, in Fig. 4 the voltage at the load is displayed and it can be seen that the amplitude of the pulse is very close to the source. The actual impedance of the created coaxial cable is  $49.2 \Omega$  which acceptable for the application.

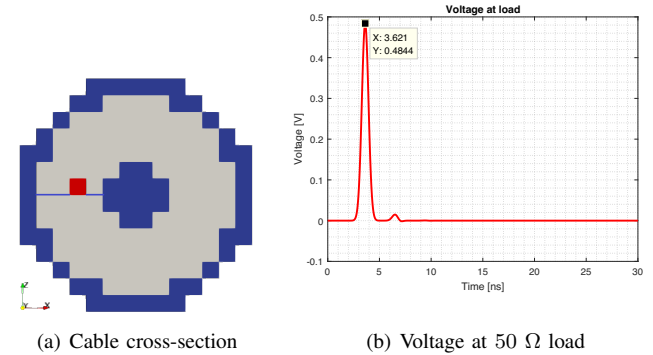


Figure 4. Coaxial cable cross section and voltage at load connected to cable

Finally the probe was built based on the dimensions of the CS610 three-rod probe and the design proposed by Heimovaraa in [21], a rendered model of the TDR probe is shown in Fig. 5. The dimensions and materials of the simulated and physical probes are shown in Table I. The designed probe was placed in different media and waveforms of the TDR response were obtained. In the following Sections V and VI the analysis of the waveforms obtained from simulation and validation of analysis is done.

#### V. TDR DATA PROCESSING

In order to recover the properties of soils from the TDR waveforms time-domain and frequency-domain analysis are due. A typical TDR waveform is as shown in Fig. 6, the analysis done to obtain the electrical properties of the soil is summarized on Fig. 3. In this section a detailed review on each of them will be done.

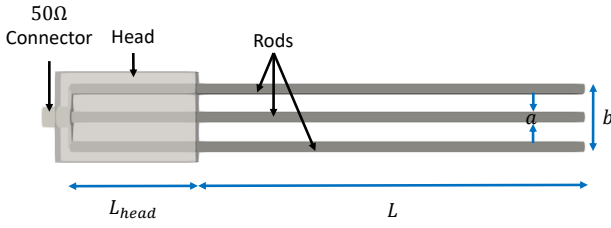


Figure 5. TDR probe design rendered in gprMax.

|                   | Campbell Scientific CS610 | Handmade epoxy       | Simulated 1         | Simulated 2         |
|-------------------|---------------------------|----------------------|---------------------|---------------------|
| $L$               | 30 cm                     | 30 cm                | 30 cm               | 30 cm               |
| $L_{head}$        | 9 cm                      | 11 cm                | 10 cm               | 10 cm               |
| $a$               | 0.48 cm                   | 0.476 cm             | 0.8 cm              | 0.4 cm              |
| $b$               | 4.5 cm                    | 4.6 cm               | 4.5 cm              | 4.5 cm              |
| Rod material      | -                         | Bronze               | Stainless steel     | Stainless steel     |
| Head material     | Epoxy resin               | Epoxy resin          | Epoxy resin         | Epoxy resin         |
| Head permittivity | $\epsilon_r = 1.79$       | $\epsilon_r = 4.6$   | $\epsilon_r = 3.6$  | $\epsilon_r = 3.6$  |
| Connector         | RG-8 cable                | Female SMA connector | 49.2Ω coaxial cable | 49.2Ω coaxial cable |

Table I

DESCRIPTION OF THE DIMENSIONS AND MATERIALS OF THE DIFFERENT PROBES USED

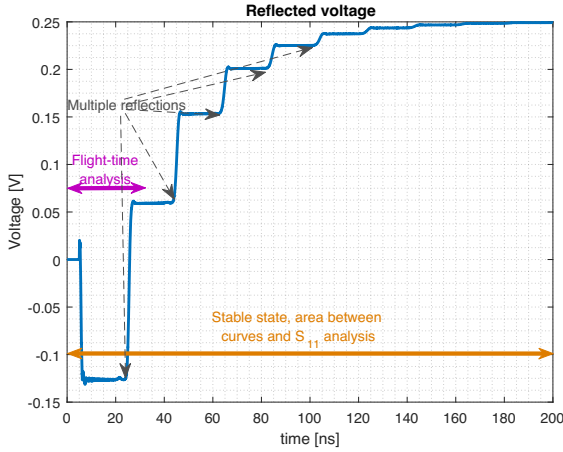


Figure 6. Reflected TDR waveform of probe immersed in deionized water.

#### A. Flight time

Flight time analysis is done over the time-domain and its aim is to find the apparent permittivity  $K_a$  of the medium where the coaxial probe is inserted. It is well-known that the propagation velocity of electromagnetic waves within a medium is determined by the permittivity and permeability of it, as presented on Eq. (10). The way Eq. (10) is presented assumes that permittivity is frequency independent, which is not accurate as shown in Section II, this expression is better described as apparent permittivity  $K_a$ . As we have assumed  $\mu_r = 1$  for all media, Eq. (10) can be rewritten as Eq. (11).

$$v_p = \frac{1}{\sqrt{\mu_0 \mu_r \epsilon_0 \epsilon_r}} = \frac{c_0}{\sqrt{\mu_r \epsilon_r}} \quad (10)$$

$$v_p = \frac{c_0}{\sqrt{K_a}} \quad (11)$$

Flight time analysis is done based on: the knowledge of the length of the probe ( $L$ ) and therefore the travelled distance

( $D$ ) by an electromagnetic wave inside it; and the ability to determine the time it takes for the electromagnetic wave to travel said length ( $\Delta t$ ). Through the definition of propagation velocity on Eq. (11),  $K_a$  can be related with  $D$  and  $\Delta t$ . Often the distance traveled by the wave is taken as  $D = 2L$  as measurements are done over one port and this corresponds to the two-way travelled distance, but in some cases it is also presented as  $D = L$ . One must be aware of the way the data is presented in order to have an accurate description of  $K_a$ , to avoid misunderstandings the equation to determine  $K_a$  is presented in terms of  $D$  in Eq. (12).

$$K_a = \frac{c_0^2}{v_p^2} = \frac{c_0^2 \Delta t^2}{D^2} \quad (12)$$

The procedure to systematically determine  $\Delta t$  used in this paper is based on the procedure proposed by Heimovaara and Bouting [26], with some additional data-based criteria in the selection of time intervals and with a different method to calculate the tangent lines that determine the end-reflection point.

Flight time is determined by locating the start- and end-point of the reflected waveform as  $\Delta t = t_{end} - t_{start}$ . The start-point is when the wave enters the probe rods inserted on the medium to characterize and the end-point is when the reflected wave reaches the port. To determine the start-point of the reflected waveform a time-gating technique is used as the time of the wave over the coaxial cable ( $t_{cable}$ ) and over the probe header ( $t_{head}$ ) are known, all the values for the reflected waveform are set to zero over the time interval  $t_{cable} + t_{head}$ , the first non-zero value after this time interval is taken as the start-point  $t_{start}$ . The end-point is calculated by locating the inflection point (S-point) of the first reflection caused by the end of the probe, this is done through the first derivative of the reflected waveform. The end-point is where two tangent lines to the curve intersect, one to the S-point and one to the base before the rise due to the reflection. The analysis done for location of the end-point for this waveform is shown in Fig. 7. Results from flight time analysis can be viewed on the waveform as in Fig. 9.

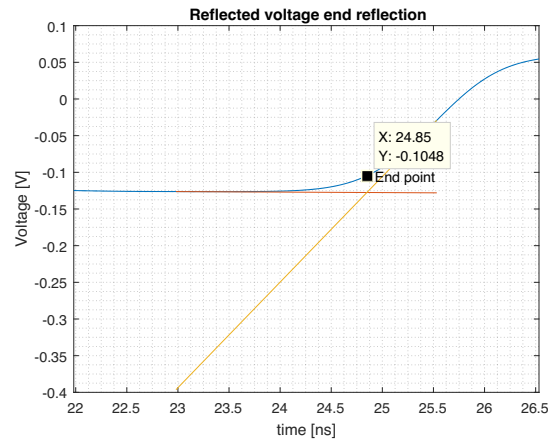


Figure 7. Location of end-point.

### B. Stable state amplitude

Stable state amplitude analysis gives the conductivity of the medium using Eq. (13) proposed by Giese and Tiemann [27], in which  $\rho_\infty = v_{ref}(\infty)/v_{inc}(\infty)$  is the reflection coefficient in stable state. Results from stable state amplitude analysis can be viewed on the waveform as in Fig. 10.

$$\sigma_{DC} = \frac{\varepsilon_0 c_0}{zL} \left( \frac{1 - \rho_\infty}{1 + \rho_\infty} \right) \left[ \frac{\text{S}}{\text{m}} \right] \quad (13)$$

### C. Area between theoretical and actual reflections

Area between theoretical and actual reflections is used to determine the static permittivity  $\varepsilon_s$  for relaxation models similar to the Havriliak-Negami model. This analysis was first proposed by Giese and Tiemann [27] and it is the base for the analysis done in this paper. A minor modification was made introducing a form factor constant:  $g$ , to compensate for the mismatch from the probe behavior and an actual coaxial line. The new equation proposed to obtain  $\varepsilon_s$  is presented in Eq. (14) where  $A$  is the surface area between a theoretical waveform for  $\varepsilon_s^*(f) = 1 - j\sigma_{DC}/(2\pi f \varepsilon_0)$  and the actual waveform. The form factor constant is obtained through calibration with materials of known  $\varepsilon_s$ . Results from area between reflection waveforms analysis can be viewed on the waveform as in Fig. 11.

$$\varepsilon_s = \frac{A \cdot c_0}{g \cdot v_{ref}(\infty) \cdot zL} + 1 \quad (14)$$

### D. $S_{11}$ scattering parameter

To obtain the  $S_{11}$  parameter from the TDR measurements, the incident and reflected waveforms must be transformed into the frequency domain. As both signals are discrete, the Discrete Fourier Transform (DFT) can be applied. However, the DFT of a step function contains errors because the algorithm assumes a step to zero at the end of the signal [19]. In order to transform  $v_{inc}$  and  $v_{ref}$  properly, the first derivative of the functions  $v'_{inc}$  and  $v'_{ref}$  are used because of the property of the DFT given in Eq. (15). Then the  $S_{11}$  parameter of the TDR can be calculated by Eq. (16). Equations (5) - (9) can be used to determine  $\varepsilon^*(f)$  through an optimization method, using  $S_{11}$  obtained from measurements. Measured  $S_{11}$  produces a signal similar to the one in Fig. 12.

$$X(f) = DFT[x(t)] = \frac{\Delta t}{1 - \exp(-j2\pi f \Delta t)} DFT[x'(t)] \quad (15)$$

$$S_{11} = \frac{DFT[v_{ref}(t)]}{DFT[v_{inc}(t)]} = \frac{DFT[v'_{ref}(t)]}{DFT[v'_{inc}(t)]} \quad (16)$$

### E. PSO algorithm for $\varepsilon^*(f)$ retrieval

Once all the analysis presented above is done for the TDR waveforms,  $\varepsilon^*(f)$  can be recovered from Eqs. (5) - (9) with a numerical method that finds the best fit between theoretical and the measured scattering parameter. The method here presented is Particle Swarm Optimization (PSO), a heuristic algorithm that mimics the behavior of a group of animals in search for food. The theoretical framework to develop the algorithm was taken from Kelley et al. [16].

PSO models potential solutions as a group of particles in a multidimensional space, where each dimension is the span of values a particular parameter can take. Solutions that result from the PSO algorithm are Debye model parameters that describe  $\varepsilon^*(f)$ , at this point some of the parameters of the Debye model are already known from the time-domain analysis:  $\varepsilon_s$  and  $\sigma_{DC}$ . The unknown parameters:  $\varepsilon_\infty$  and  $\tau_0$  are the dimensions that make up the space where the particles will look up for solutions. The developed algorithm places 800 particles in random locations of the 2-dimensional space, constraints are given for the initial random position so the particles are spread over what could be considered realistic solutions for soil characterization ( $\varepsilon_\infty \in [1, 5]$  and  $\tau_0 \in [10 \times 10^6, 20 \times 10^9]$  Hz).

Once every particle is located, an iterative process begins, the theoretical scattering function is built with the Debye model that each particle describes. Number of peaks in the  $S_{11}$  scattering parameter is the criteria used when comparing the solutions generated by the particle swarm with the measured scattering function. The best fitness that each particle generates ( $pBestFitness$ ) is stored along with the position of the particle where the best fitness was obtained ( $pBest$ ). After the fitness of all particles is evaluated the best overall fitness from the swarm is stored ( $gBestFitness$ ) and the position of the particle that generated the fitness is stored too ( $gBest$ ). Each particle will move with a given velocity that is calculated using Eq. (17); where  $v$  is the velocity of each particle,  $x$  is the current position of each particle,  $M, N \sim U[0, 1]$  are random variables, and  $w = 0.5$ ,  $c_1 = 1.4$  and  $c_2 = 1.4$  are weight parameters used to control the progression of the algorithm.

$$v = wv + c_1 \cdot M \cdot (pBest - x) + c_2 \cdot N \cdot (gBest - x) \quad (17)$$

Algorithm is set to run 50 iterations after which the location that generated the best overall fitness is selected as the answer for  $\varepsilon^*(f)$ . In Fig. 13, the placement of particles for given iterations is shown. Solutions are constrained, as no negative frequencies are valid for the solution and the soils cannot have values of  $\varepsilon_\infty < 1$  or  $\varepsilon_\infty > \varepsilon_s$ . If one of this conditions is not met for a particle, said particle is located on a random position for the next iteration. The whole PSO algorithm is ran 10 times and the final parameters are the mean from all  $gBest$  answers. The solution obtained with the algorithm recovers the  $S_{11}$  parameter, as shown in Fig. 14, and the complex permittivity associated to it, as shown in Fig. 15.

## VI. VALIDATION OF TDR PROCESSING

Validation of the processing algorithms is done with simulated TDR responses on probes buried in media. Electrical properties of five media used for validation are described in Table II under the “Input” columns (note that  $K_a$  is not a parameter in the Debye relaxation model so the theoretical value is not available for comparison). The probe used for the validation is the one referred as “Simulated 1” in Table I. Waveforms for Medium A are displayed on this Section in Figures 8 to 15 and the results of the algorithm for the media are given in Table II under the “Recovered” columns.

| Medium:           | A       |                        | B       |           | C        |           | D        |                        | E       |                       |
|-------------------|---------|------------------------|---------|-----------|----------|-----------|----------|------------------------|---------|-----------------------|
| Parameters        | Input   | Recovered              | Input   | Recovered | Input    | Recovered | Input    | Recovered              | Input   | Recovered             |
| $\epsilon_s$      | 30      | 30.0021                | 25.2    | 30.2309   | 30.3     | 30.7624   | 26.5     | 17.2759                | 79.9    | 76.019                |
| $\epsilon_{inf}$  | 5       | 3.9927                 | 4.52    | 5.8310    | 5.3      | 4.1713    | 2.68     | 2.759                  | 4.22    | 2.32                  |
| $f_{relax}$       | 800 MHz | 801.2 MHz              | 124 MHz | 106 MHz   | 17.3 GHz | 12.22 GHz | 1.12 GHz | 1.15 GHz               | 17 GHz  | 17.7 GHz              |
| $T_0$             | 199 ps  | 198.65 ps              | 1.27 us | 1.50 us   | 9.2 ps   | 13.02 ps  | 142 ps   | 138.39 ps              | 9.36 ps | 8.99 ps               |
| $\Sigma_{DC} S/m$ | 0       | -1.94x10 <sup>-7</sup> | 0.00992 | 0.0073    | 0.003    | 0.0022    | 0        | -1.66x10 <sup>-7</sup> | 0       | 2.58x10 <sup>-5</sup> |
| K <sub>a</sub>    |         | 26.4658                |         | 15.1187   |          | 32.692    |          | 26.5854                |         | 83.6034               |

Table II  
SIMULATED AND RECOVERED ELECTRICAL PROPERTIES OF VALIDATION MEDIA.

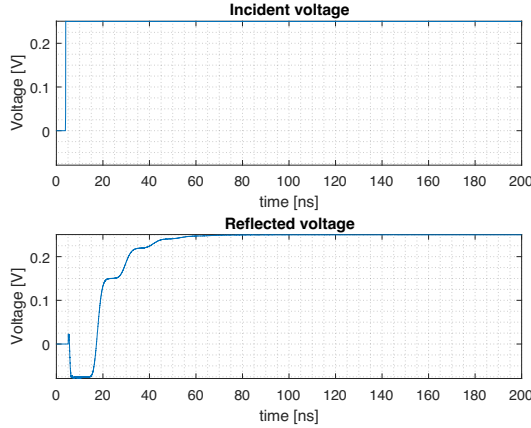


Figure 8. TDR incident and reflected waveforms by probe immersed in Medium A.

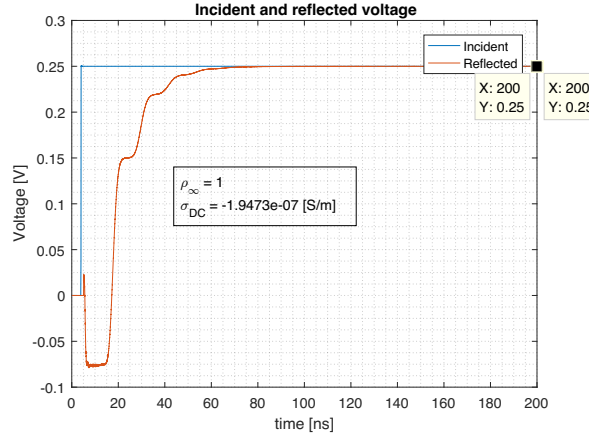


Figure 10. Conductivity ( $\sigma_{DC}$ ) analysis for Medium A.

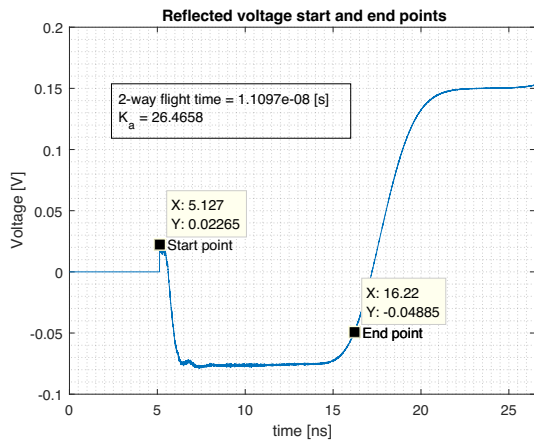


Figure 9. Apparent permittivity ( $K_a$ ) analysis for Medium A.

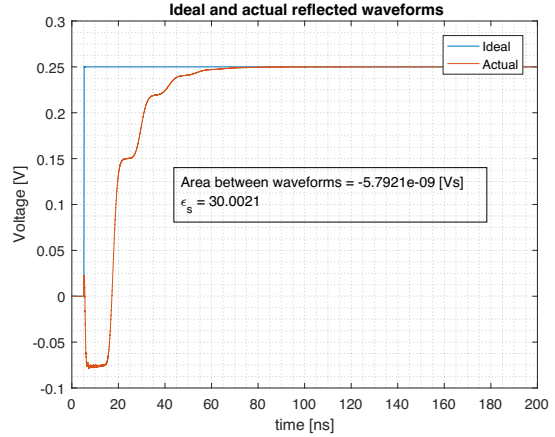


Figure 11. Static permittivity ( $\epsilon_s$ ) analysis for Medium A.

## VII. TDR MEASUREMENT OF COLOMBIAN SOILS

Field measurements allow the knowledge of electrical properties from real Colombian soils. TDR equipment used for field measurements is Campbell Scientific TDR200 [22] along with two TDR probes: Campbell scientific CS610 [23] and a handmade probe based on the design proposed by Heimovaara [21]; dimensions and materials of the probes are shown in Table I and pictures of the buried probes are shown in Fig. 17. Waveforms measured with both probes are very similar and the resulting complex permittivity recovered from them is

similar as well.

Soils from five different locations in Colombia were selected—to be characterized—with consideration of including varied environments, weather, mineralogy and geography. Map in Fig. 16 shows the location of the selected soils. Table III shows the description of them (taken from Agustin Codazzi Geographic Institute [28]) and the temperature of the environment when taking the measurements.

Results of soil characterization are given in Table IV. Figure 17 shows the probes buried on two of the five measurement sites.

|                                 | <b>San Alberto Magno</b>  | <b>Hacienda el Noviciado</b>  | <b>Ubaté</b>  | <b>San Miguel de Sema</b>   | <b>La Candelaria Desert</b>                  |
|---------------------------------|---|---|---|---|--|
| <b>Sand fraction mineralogy</b> | Feldspars - Volcanic Glass<br>Amphiboles - Quartz (FVAQ)                                  | Quartz - Feldspars<br>Amphiboles (QFA)                                    | Quartz - Feldspars<br>Amphiboles (QFA)  | Quartz - Feldspars<br>Amphiboles - Volcanic Glass<br>Altered (QFAVAL)               | Quartz - Feldspars<br>Altered (QFAL)         |
| <b>Clay fraction mineralogy</b> | Montmorillonite - Kaolinite (MTK)   | Kaolinite - Micas<br>Allophane (KMA)                                      | Kaolinite - Micas<br>Allophane (KMA)  | Kaolinite - Micas<br>Quatz (KMQ)  | Kaolinite - Micas<br>Quatz (KMQ)             |
| <b>Vegetation and usage</b>     | Managed pastures<br>Areas with civil work, weed control and fertilization                 | Miscellaneous<br>Areas with transient, perennial and semi-perennial crops | Managed pastures<br>Areas with civil work and paddock distribution and rotation           | Managed pastures<br>Areas with dense pastures and paddock distribution and rotation | Pajonales and areas without vegetation cover |
| <b>Soil description</b>         | Soils from very cold climates, humid to very humid, in paramo areas, acid and desaturated | Soils developed in depressed and flooded areas of all climates            | Soils from very cold climates, humid to very humid, in paramo areas, acid and desaturated | Soils developed in depressed and flooded areas of all climates                      | Severely eroded areas                        |
| <b>Meas. temperature [°C]</b>   | 16  | 17  | 12  | 17  | 22   |

Table III  
DESCRIPTION OF THE MEASUREMENT AREAS

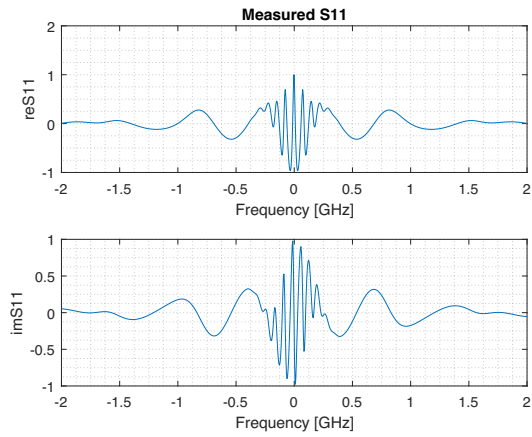


Figure 12. Measured  $S_{11}$  for Medium A.

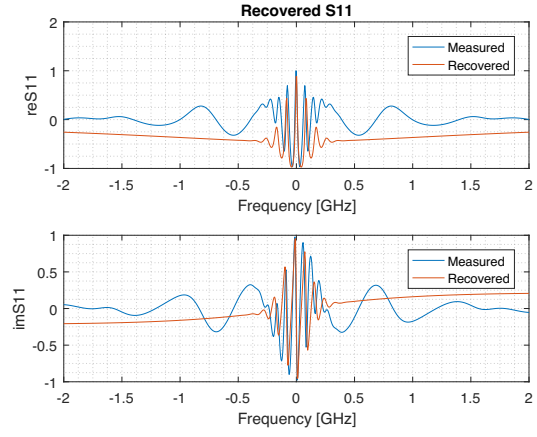


Figure 14. Recovered  $S_{11}$  vs. Measured  $S_{11}$  for Medium A.

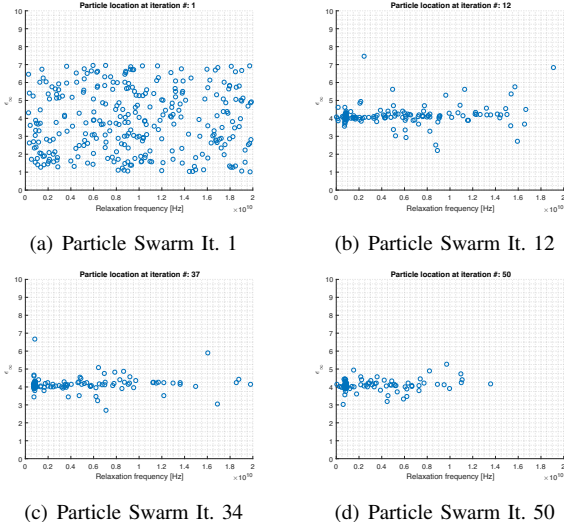


Figure 13. Particles location in the 2-dimensional space on different iterations.

|                      | <b>San Alberto Magno</b> | <b>Hacienda el Noviciado</b> | <b>Ubaté</b> | <b>San Miguel de Sema</b> | <b>La Candelaria Desert</b> |
|----------------------|--------------------------|------------------------------|--------------|---------------------------|-----------------------------|
| $\varepsilon_s$      | 14.62                    | 29.8685                      | 6.7487       | 30.8998                   | 35.1896                     |
| $\varepsilon_\infty$ | 4.156                    | 3.708                        | 4.0838       | 3.76446                   | 4.2156                      |
| $f_{relax}$          | 2.4875 GHz               | 9.6862 GHz                   | 6.6423 GHz   | 873.26 MHz                | 595.19 MHz                  |
| $\tau_0$             | 63.98 ps                 | 16.43 ps                     | 23.96 ps     | 182.25 ps                 | 267.4 ps                    |
| $\sigma_{DC}$ [S/m]  | 0.0074                   | 0.0081                       | 0.0068       | 0.0060                    | 0.0011                      |
| $R_a$                | 25.6404                  | 14.2292                      | 8.0144       | 27.7512                   | 8.2224                      |

Table IV

COLOMBIAN SOIL PARAMETERS OF COMPLEX PERMITTIVITY FOR DEBYE RELAXATION MODEL.

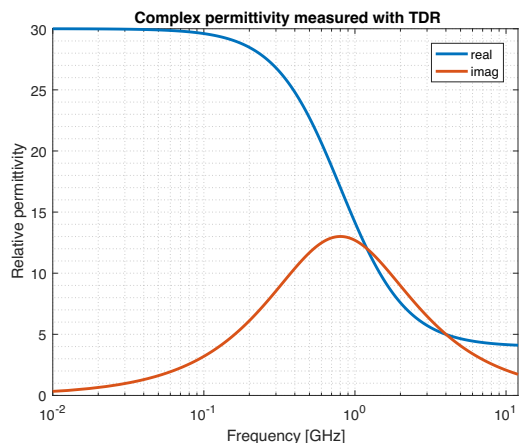


Figure 15. Recovered complex permittivity for Medium A.

## VIII. IDENTIFICATION AND CONSTRUCTION OF IED IN GPRMAX

For simulations of IED detection with GPR to accurately represent the Colombian scenarios, an IED was built into gprMax. IED in Fig. 18 is the reference for the built IED. External configuration of this IED consist of a cylindrical casing with a plastic syringe on top as triggering mechanism. Explosives for this type of IED are various such as: Ammonium Nitrate, ANFO, ALANFO, R1, hydro-gels,

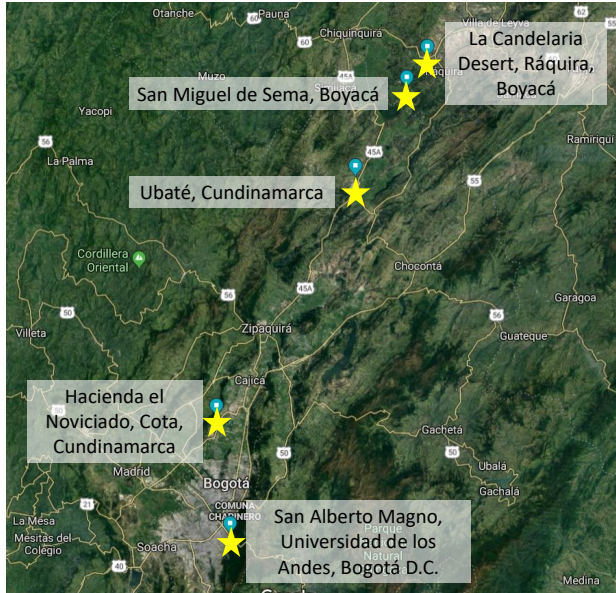


Figure 16. Map of measurement locations in Colombia. *Location and map taken with Google Maps App*



(a) Campbell Scientific CS610 buried in La Candelaria desert.  
(b) Handmade epoxy probe buried in San Miguel de Sema.

Figure 17. TDR probes buried in two of the characterized soils.

emulsions, nitroglycerin and TNT [2], [3], [29]. IEDs have many configurations and non-standard sizes [2], [3], [29], so the built model includes variable parameters such as: size, enclosure and explosive materials, and triggering mechanisms (electrical and chemical triggers).

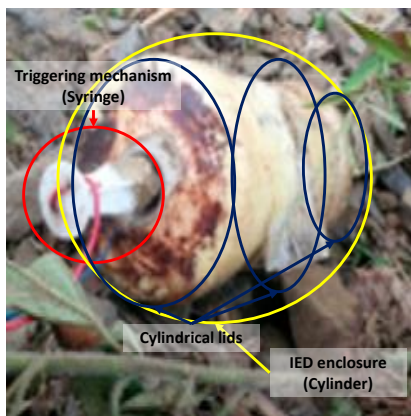


Figure 18. Geometric identification of IED. Photography taken from [3].

The built IED, rendered from gprMax with different material configurations and sizes is shown in Fig. 19. This IED model allows to modify the diameter of the casing, the height of the IED, the triggering mechanism (electric and chemical), the inclusion and size of metallic and non-metallic shrapnel, and the explosive electrical description. Simulation in Section IX uses one configuration of this IED for San Alberto Magno soil description presented in Table IV.

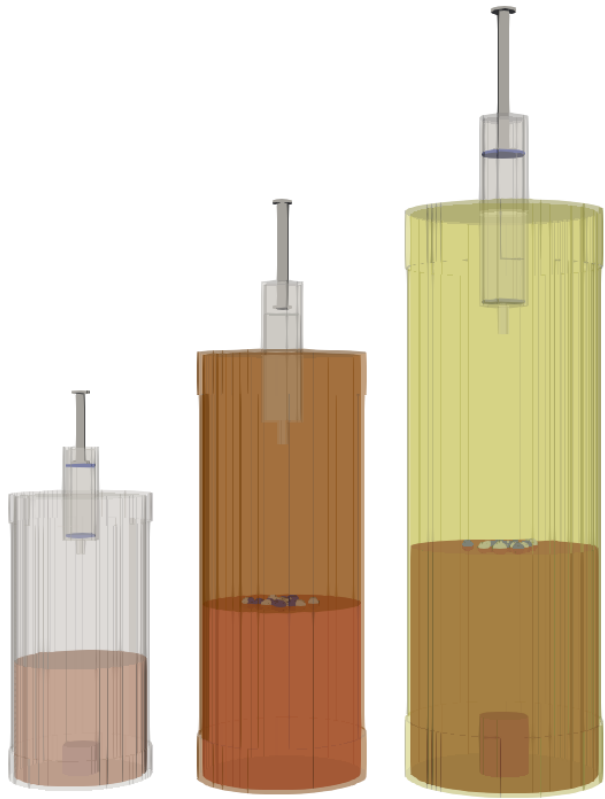


Figure 19. IED model built in gprMax with different size, materials and trigger configurations.

## IX. GPR SIMULATION ON COLOMBIAN CONDITIONS

Characterization made with TDR can be used to simulate IED detection scenarios with GPR. The Debye model integrates seamlessly with the FDTD algorithm through its Fourier transform [16], [30], gprMax includes the Debye model as a default command, so the soils from Table IV can be inserted easily to a simulated scenario. Using the created IED model a detection scenario is set up using hertzian dipoles as the GPR antennas as shown in Fig. 20. Detection results are shown as a B-Scan, taken over the middle of the soilbox, in Fig. 21. The simulated scenario uses an IED with PVC enclosure, ANFO as explosive and an electric triggering mechanism; the soil used is San Alberto Magno soil described on Table IV.

B-Scan from Fig. 21 show that the IED reflection is perceived by the antennas right at the middle of the measurement scenario, as expected. The signal from the IED is blurry and of very low power compared with the signal reflected

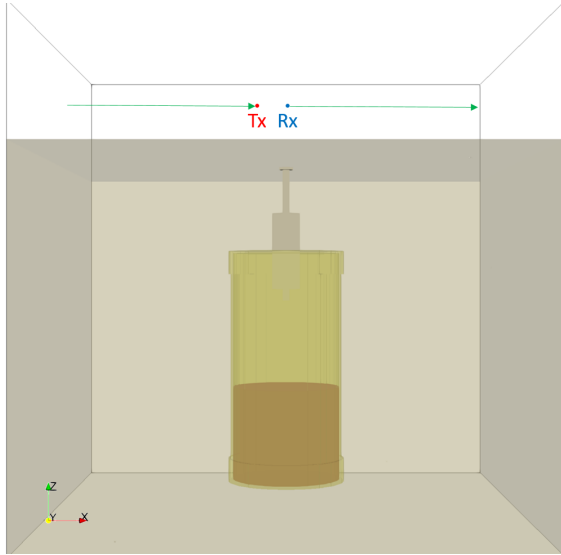


Figure 20. Detection scenario with IED buried in San Alberto Magno soil.

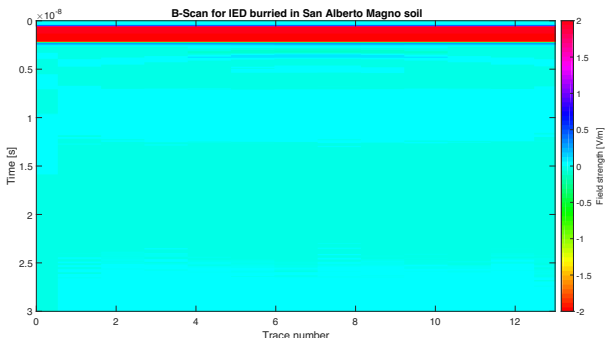


Figure 21. B-Scan obtained from Fig. 20 survey.

by the soil, but with different GPR calibration methods and with image processing algorithms the IED should be detected effectively. This type of simulation can be reproduced with different configurations of IEDs and soils in order to determine the effectiveness of GPR in varying scenarios.

## X. CONCLUSION

The applied TDR technique and the algorithms developed for it, are a powerful tool to determine the electrical properties of soils for a wide frequency band; having these soil properties is important for the reproduction of actual IED detection scenarios with GPR in simulation. A GPR benchmarking tool can be created from recovering the electrical properties of soils; either by reproduction of soil electrical characteristics in lab or by creating simulated scenarios and building antenna models into the simulator. The seamless integration of the obtained soil characterization and Debye relaxation model (included in gprMax), allow efficient scenario creation; this along with the open-source approach of gprMax to create modules and objects with different geometries, make this simulator a very useful tool for GPR humanitarian demining applications. Many simulations can be made with gprMax:

placing IED in different depths and positions, using different descriptions of soil and configuring many more variables to obtain a good database that could perhaps be used as a machine learning dataset.

The recovered complex permittivity shows that apparent permittivity is not an accurate description of the actual permittivity of the media. Comparing  $K_a$  values with the Debye model parameters leads to the conclusion that for some materials, with relaxation frequencies near to 1 GHz,  $K_a$  is very close to  $\varepsilon_s$  (at least for the pulse with 85 ps rise time). For materials with lower relaxation frequencies,  $K_a$  seems to take values under  $\varepsilon_s$ , and for materials with higher relaxation frequencies,  $K_a$  seems to take values over  $\varepsilon_s$ . Measurements with pulses of different rise times could be useful to determine the behavior of  $K_a$  vs.  $\varepsilon_s$  for materials with different relaxation frequencies. Form factor ( $g$ ) compensation proved to be useful for the made validation measurements. This can be considered as an enhancement to the previously used formula for  $\varepsilon_s$  calculation.

Information on the relaxation frequency might be determined from the time-domain waveform analysis, as media with higher relaxation frequency showed longer settling times for the waveform to reach stable state. In the state of the art review, no clear relationship between these parameters was found so finding it could prove to be a good addition to the TDR theoretical framework.

Measurements with TDR proved to be time consuming as the procedure to bury and pull the probes out of the soil is quite troublesome. Probes have to be handled with care as changes in rod separation or dents may alter the measurements, but even when pre-probing the holes on the ground the bury/pull-out procedure requires to apply strength in them. The force applied to the probes can be reduced by using shorter probes, sacrificing measurement volume but eventually covering more area by saving time. One advantage that the handmade probe had over the CS610 probe was having no attached cable but an SMA connector, as the burying of the probes required them to be hit on the head with a plastic mallet. When hitting the CS610 probe one must be careful to not hit the cable, hitting with less strength and not directly on the center, making the burying process much slower. An enhanced probe header design can be made, where the burying and pull-out procedure is done faster without fearing to damage the probes. By not having a fixed cable attached to the probe, the cable for the handmade probe is easier to carry, can be replaced if damaged and can be of any length suitable for the application; collected waveforms show that the results from both probes agree so the impedance mismatch that the connector may cause is of little influence compared to the benefits of having a detachable cable.

Electrical characterization made with TDR can be complemented with measurements of mechanical properties of the soil. This could allow to test some empirical models that relate mechanical attributes of the soil with electrical properties and adjust the models for soils relevant to humanitarian demining in Colombia.

## REFERENCES

- [1] D. J. Daniels, *Ground penetrating radar*. IET, 2004, vol. 1.
- [2] J. M. H. Hendrickx, A. Molina, D. Diaz, M. Grasmueck, H. A. Moreno, and R. D. Hernández, "Humanitarian IED clearance in Colombia," *SPIE Defense and Security Symposium*, vol. 2, no. 1, p. 69530C, 2008.
- [3] P. A. Prada and M. Chávez Rodríguez, "Demining Dogs in Colombia - A Review of Operational Challenges, Chemical Perspectives, and Practical Implications," *Science and Justice*, vol. 56, no. 4, pp. 269–277, 2016.
- [4] M. Sato and K. Takahashi, "Development of the Hand held dual sensor ALIS and its evaluation," *2007 4th International Workshop on Advanced Ground Penetrating Radar*, pp. 3–7, 2007.
- [5] M. Sato, K. Takahashi, and J. Fujiwara, "Hand held dual sensor ALIS and its evaluation test in Cambodia," *International Geoscience and Remote Sensing Symposium (IGARSS)*, pp. 18–21, 2007.
- [6] M. Sato, K. Kikuta, and R. Bustamante Miller, "Evaluation of ALIS GPR for Humanitarian Demining in Colombia and Cambodia," in *Proceedings of the 2018 20th International Conference on Electromagnetics in Advanced Applications, ICEAA 2018*, 2018.
- [7] I. Giannakis, A. Giannopoulos, and C. Warren, "A Realistic FDTD Numerical Modeling Framework of Ground Penetrating Radar for Landmine Detection," *IEEE Journal of Selected Topics in Applied Earth Observations and Remote Sensing*, vol. 9, no. 1, pp. 1–15, 2015.
- [8] J. Igel, "The Small-Scale Variability of Electrical Soil Properties - Influence on GPR Measurements," *12th International Conference on Ground Penetrating Radar*, p. 10, 2008.
- [9] C. Balanis, *Advanced Engineering Electromagnetics*. Wiley, 2012.
- [10] J. Igel, "On the Small-Scale Variability of Electrical Soil Properties and Its Influence on Geophysical Measurements," Ph.D. dissertation, Goethe University Frankfurt, 2007.
- [11] D. A. Robinson, S. B. Jones, J. M. Wraith, D. Or, and S. P. Friedman, "A Review of Advances in Dielectric and Electrical Conductivity Measurement in Soils Using Time Domain Reflectometry," *Vadose Zone Journal*, vol. 2, no. 1996, pp. 444–475, 2003.
- [12] S. B. Jones and D. Or, "Frequency Domain Analysis for Extending Time Domain Reflectometry Water Content Measurement in Highly Saline Soils," *Soil Science Society of America Journal*, 2004.
- [13] D. A. Robinson, M. G. Schaap, D. Or, and S. B. Jones, "On the effective measurement frequency of time domain reflectometry in dispersive and nonconductive dielectric materials," *Water Resources Research*, vol. 41, no. 2, pp. 1–9, 2005.
- [14] P. Debye, "Polar Molecules," *Journal of the Society of Chemical Industry*, vol. 48, no. 43, pp. 1036–1037, 1929.
- [15] K. S. Cole and R. H. Cole, "Dispersion and absorption in dielectrics i. alternating current characteristics," *The Journal of Chemical Physics*, vol. 9, no. 4, pp. 341–351, 1941.
- [16] D. F. Kelley, T. J. Destan, and R. J. Luebbers, "Debye function expansions of complex permittivity using a hybrid particle swarm-least squares optimization approach," *IEEE Transactions on Antennas and Propagation*, vol. 55, no. 7, pp. 1999–2005, 2007.
- [17] A. Giannopoulos, "Modelling ground penetrating radar by GprMax," *Construction and Building Materials*, vol. 19, no. 10, pp. 755–762, 2005.
- [18] D. Castro Malagón, R. Siachoque Bernaluy, and J. Serna Giraldo, *El ABC de los suelos para no expertos*. Subdirección de Agrología Instituto Geográfico Agustín Codazzi, 2010, vol. 1.
- [19] T. J. Heimovaara, "Frequency domain analysis of time domain reflectometry waveforms - 1. Meurement of the complex dielectric permittivity of soils," *Water Resources Research*, vol. 30, no. 2, pp. 189–199, 1994.
- [20] K. C. Yaw(Rohde&Schwarz), "Measurement of dielectric material properties Application Note," *Measurement Techniques*, pp. 1–35, 2006.
- [21] T. J. Heimovaara, "Design of triple wire time domain reflectometry probes in practice and theory," *Soil Science Society of America journal*, vol. 57, pp. 1410–1417, 1993.
- [22] Campbell Scientific, "Instruction Manual: TDR200-Based Time-Domain Reflectometry System," 2016.
- [23] ——, "CS610-L 3-Rod TDR Probe with RG8 Cable," 2018.
- [24] J. G. Maloney, K. L. Shlager, and G. S. Smith, "A Simple FDTD Model for Transient Excitation of Antennas by Transmission Lines," *IEEE Transactions on Antennas and Propagation*, 1994.
- [25] Pasternack, "Flexible RG8 Coax Cable Single Shielded with Black PVC Jacket," pp. 1–3.
- [26] T. Heimovaara and W. Bouten, "A Computer-Controlled 36-Channel Time Domain Reflectometry System for Monitoring Soil Water Contents," *Water Resources Research*, vol. 26, no. 10, pp. 2311–2316, 1990.
- [27] K. Giese and R. Tiemann, "Determination of the complex permittivity from thin-sample time domain reflectometry improved analysis of the step response waveform," *Advances in Molecular Relaxation Processes*, vol. 7, no. 1, pp. 45–59, 1975.
- [28] D. Castro Malagón, C. Pulido Roa, R. D. Llinás Rivera, C. Chamorro Bello, and J. Fernández Lamus, *Suelos de Colombia: origen, evolución, clasificación, distribución y uso*. Subdirección de Agrología Instituto Geográfico Agustín Codazzi, 1995, vol. 1.
- [29] Comando General Fuerzas Militares de Colombia, "Testigos Fieles - Victimas del Horror de las Minas Antipersonal," p. 274, 2008.
- [30] M. Loewer and J. Igel, "FDTD Simulation of GPR with a Realistic Multi-Pole Debye Description of Lossy and Dispersive Media," in *International Conference of Ground Penetrating Radar (GPR)*, 2016, pp. 3–7.